Ignition, combustion modes and NO/N2O emissions in ammonia/n-heptane combustion under RCCI engine conditions

Zhou, Yuchen; Xu, Shijie; Xu, Leilei; Bai, Xue-Song

Published in:
Combustion and Flame

DOI:
10.1016/j.combustflame.2025.114352

2025

Document Version:
Publisher's PDF, also known as Version of record

Combustion and Flame 280 (2025) 114352

Contents lists available at ScienceDirect

Combustion and Flame

journal homepage: www.sciencedirect.com/journal/combustion-and-flame

Ignition, combustion modes and NO/N_2O emissions in ammonia/n-heptane combustion under RCCI engine conditions

Yuchen Zhou, Shijie Xu, Leilei Xu, Xue-Song Bai *

Department of Energy Sciences, Lund University, Lund, 22100, Sweden

ARTICLE INFO

Keywords:
Ammonia marine engine
Direct numerical simulation
Combustion modes
Reactivity-controlled compression ignition
NO and N_2O emissions

ABSTRACT

Ammonia has been considered a promising carbon-free fuel for marine engines. However, its low flame speed and high nitrogen oxides (NO_x) and nitrous oxide (N_2O) emissions present significant challenges. To address these issues, novel combustion concepts, such as ammonia/diesel dual-fuel Reactivity-Controlled Compression Ignition (RCCI) engines, have been proposed. This paper presents a detailed investigation of ammonia/n-heptane combustion under RCCI engine conditions using direct numerical simulation (DNS) to gain insights into ignition, combustion modes, and emission formation mechanisms. A temporally evolving jet configuration is considered in the DNS, with the computational domain comprising two regions: a fuel-lean premixed ammonia/air mixture and a fuel-rich n-heptane jet/ammonia/air mixing region. The pressure and temperature in these regions are representative of typical marine engine operating conditions. The DNS results reveal multiple reaction layers, including the fuel-lean premixed flame (LPF), fuel-rich premixed flame (RPF), diffusion flame (DF), and rich ammonia oxidation layer (RAOL). The LPF propagates into the ambient ammonia/air mixture, significantly influencing combustion efficiency and NO formation, while the RPF propagates into the fuel-rich n-heptane/ammonia/air mixture due to low-temperature ignition. The DF oxidizes combustion intermediates and NO, while the RAOL facilitates ammonia oxidation, forming intermediate species such as hydrogen (H_2), amino radicals (NH_2), and nitrene radicals (NH), which eventually participate in the reactions in the DF and RPF. The back-supported propagation of the LPF is influenced by n-heptane mixing, heat, and radical transfer from the DF, and jet-induced vortices and turbulence. Increasing n-heptane jet speed enhances this effect, improving ammonia combustion efficiency. NO primarily forms in the LPF and is consumed in the DF, while N_2O is generated in the LPF (continuously) and RPF (during the ignition stage), while being consumed in the RAOL. Higher n-heptane jet velocity accelerates NO consumption but increases N_2O formation due to enhanced mixing and ammonia entrainment. Understanding these mechanisms provides valuable insights into optimizing RCCI combustion for reduced emissions and improved efficiency in ammonia-fueled marine engines.

Novelty and significance statement

• This research investigates ammonia-fueled RCCI engines using high-fidelity direct numerical simulations, examining the effects of turbulent jets and ambient ammonia concentration. The simulations resolve all fine structures and provide detailed insights, while the findings are applicable to practical marine engine scenarios.

• Multiple reaction layers in ammonia RCCI combustion are identified, including back-supported lean premixed flame propagation, cool flame, diffusion flame, and rich ammonia oxidation layer.

• The study elucidates the processes behind NO and N_2O emissions in ammonia RCCI engines, including their generation, consumption, and potential control.

1. Introduction

Ammonia (NH_3), as a carbon-free fuel, holds significant potential for decarbonizing the transport sector [1,2]. Its combustion in the air produces nitrogen and water as primary products, avoiding carbon dioxide (CO_2) emissions. Additionally, ammonia serves as a hydrogen carrier and is considered a sustainable fuel source, ensuring long-term energy security. However, several challenges hinder the use of ammonia in internal combustion engines. These include its poor combustion

* Corresponding author.
E-mail address: xue-song.bai@energy.lth.se (X.-S. Bai).

https://doi.org/10.1016/j.combustflame.2025.114352
Received 22 March 2025; Received in revised form 14 July 2025; Accepted 14 July 2025
Available online 4 August 2025

efficiency and the generation of substantial nitrogen oxides (NO_x) emissions due to the nitrogen content in the fuel. Previous studies have demonstrated that ammonia can be utilized in spark-ignition engines, though co-firing with a small fraction of hydrogen (e.g., 10%) is often necessary to enhance combustion efficiency [3,4]. Ammonia can serve as a fuel in compression-ignition engines; however, diesel is typically required to assist with ignition. This is because ammonia-only compression-ignition engines often face ignition challenges, even at high compression ratios like 30:1 [5].

Recent research on ammonia marine engines has focused on diesel/ammonia dual-fuel compression-ignition engines, which are highly desirable as they can be adapted from the current fleet of diesel/natural gas dual-fuel engines [6]. Several studies have explored a dual-fuel concept in which ammonia is introduced into the intake manifold, forming a premixed ammonia/air mixture prior to combustion, while diesel is directly injected during the later stages of the compression stroke to ignite the premixed ammonia/air mixture [6–13]. This approach is similar to the reactivity-controlled compression-ignition (RCCI) engine concept [14], building on earlier ammonia/diesel dual-fuel engine studies by Pearsall and Garabedian [5].

For diesel/ammonia RCCI engines, minimizing diesel use and controlling emissions of NO_x, nitrous oxide (N_2O), CO_2, carbon monoxide (CO), soot, and unburned hydrocarbons are critical. Reiter and Kong [7,8] found that at full-load of their experimental engine (40 kW output), optimal overall fuel efficiency occurred with 40%–60% diesel energy share. However, further reducing diesel energy increased nitric oxide (NO) emissions. Similarly, Yousefi et al. [10] reported a decrease in combustion efficiency from 98% to 64% as the diesel energy share dropped from 100% to 60% in their engine experiments, resulting in significant ammonia slip. In a follow-up study using the same engine, Yousefi et al. [11] demonstrated the effects of splitting the diesel injection into two parts (i.e., an early injection and a main injection before top dead center (TDC)). This injection strategy can optimize both engine efficiency and NO_X emissions. Niki et al. [9] reported results similar to those of Reiter and Kong [7,8]. Additionally, they investigated the potential for reducing ammonia slip through a second diesel injection occurring 10–50 crank angle degrees after TDC. Their findings indicated that this secondary injection significantly reduces ammonia slip but results in a slight increase in N_2O emissions. Xu et al. [6] demonstrated a 320 mm bore industrial ammonia/diesel RCCI engine achieving a low diesel energy share (down to 24%) with combustion efficiencies above 90%. However, NO emissions were notably higher than those in comparable natural gas/diesel RCCI engines. Førby et al. [12] conducted ammonia/n-heptane RCCI engine experiments and found that high combustion efficiency can be achieved with an ammonia energy share of up to 98.5% when the ammonia/air mixture is near stoichiometric (i.e., with an equivalence ratio of 0.9). Notably, unburned ammonia emissions were found to decrease with increasing ammonia energy share, which contrasts with the findings of Yousefi et al. [10]. Huang et al. [15] also demonstrated that unburned ammonia emissions increase as the ammonia energy share rises in their experimental engine. Despite similar trends in combustion efficiency and emissions reported in the literature, significant variations are observed in the absolute values of these parameters in different engines under comparable diesel energy shares. This suggests that the interaction between diesel and ammonia flames in the engine is a highly complex process, strongly influenced by engine configuration and operating conditions.

The interaction between diesel and ammonia in RCCI engine combustion influences several critical aspects, including diesel ignition, flame propagation in the premixed ammonia/air mixture, emissions of NO and N_2O, and ammonia slip. Studies have consistently shown that mixing ammonia with diesel in the mixing layer of the diesel jet leads to delayed ignition of diesel [15–17], with the delay increasing as the ammonia mass fraction or energy share in the diesel/ammonia mixture rises [12,18,19]. This delay is largely chemical in origin: ammonia competes with diesel for OH radicals [18,20,21], diminishing diesel's reactivity and its role in facilitating ignition. High scalar dissipation rates (SDR), especially in turbulent combustion with diesel sprays, further exacerbate ignition delays [22].

Low combustion efficiency and high emissions of unburnt NH_3 and N_2O are likely attributed to the slow flame propagation speed of the premixed ammonia/air mixture in a diesel/ammonia RCCI engine [15,16,23]. The ammonia flame speed is enhanced by mixing it with diesel, which creates spatial stratification of equivalence ratio and reactivity. The flame propagation in the premixed ammonia/air mixture is "back-supported" by diesel. Several researchers have studied back-supported flame propagation in ammonia combustion. Tomidokoro et al. [24] investigated the laminar flame speed of an ammonia/air mixture with equivalence ratio stratification in a one-dimensional counter-flow configuration. They found that with rich-to-lean equivalence ratio stratification, the laminar flame speed could be improved by 40% compared to the homogeneous mixture, while lean-to-rich stratification resulted in a 20% decrease in laminar flame speed. Chi and Thévenin [25] conducted direct numerical simulations (DNS) of ammonia/air combustion back-supported by a hydrogen/air jet flame in a pre-chamber/main chamber combustion system. Their results showed that the local flame displacement speed could be up to ten times faster than the ammonia/air flame speed.

Fundamental investigations into reaction zone structures, back-supported flame propagation, and the mechanisms of NO_x, N_2O, and ammonia emissions in ammonia/diesel RCCI combustion remain limited. Much of the fundamental knowledge of RCCI combustion originates from research on other fuels, such as methane [26,27], iso-octane [28,29], and methanol [30]. For example, Yu et al. [28] and Bhagatwala et al. [29] explored iso-octane/air mixtures ignited by n-heptane jets, noting that ignition typically begins within the mixing layer. This process is often followed by either premixed flame propagation or ignition wave phenomena, with the primary fuels predominantly combusted through flame propagation.

To the best of the authors' knowledge, there are no DNS studies of diesel/ammonia RCCI combustion under engine-relevant conditions. The fundamental ignition, combustion, and emission processes in diesel/ammonia RCCI engines remain poorly understood. This paper aims to bridge this gap. A typical diesel/ammonia/air stratified mixture configuration is considered, akin to the work of Zhao et al. [31], which was limited to one-dimensional laminar flame conditions. The DNS results are utilized to provide insights into the following: (a) the ignition of diesel/ammonia mixture within the mixing layer and the factors that influence the ignition process, (b) the combustion modes in RCCI combustion, (c) the back-supported flame propagation, and (d) the mechanisms underlying NO and N_2O emissions in RCCI combustion.

2. Computational setup

2.1. DNS configuration

The DNS configuration represents an idealized scenario of diesel/ammonia RCCI combustion under engine-relevant conditions, replicating critical features of RCCI engines when the pistons approach the TDC. Fig. 1 illustrates essential details of the computational domain and boundary conditions in the DNS configuration. The domain is filled with a premixed ammonia/air mixture at typical post-compression stroke temperature and pressure conditions. The computational domain has dimensions of $4L$ in the streamwise (x-) direction, $16L$ in the cross-flow (y-) direction, and L in the spanwise (z-) direction.

At the center of the domain, an n-heptane (C_7H_{16}) jet is introduced to simulate diesel spray injection into the premixed ammonia/air mixture. The n-heptane gas stream mixes with the premixed ammonia/air mixture within a region characterized by a width H.

For the domain boundaries, periodic boundary conditions are applied in the streamwise (x-direction) and spanwise (z-direction) boundaries. A non-reflective outflow boundary condition is implemented for

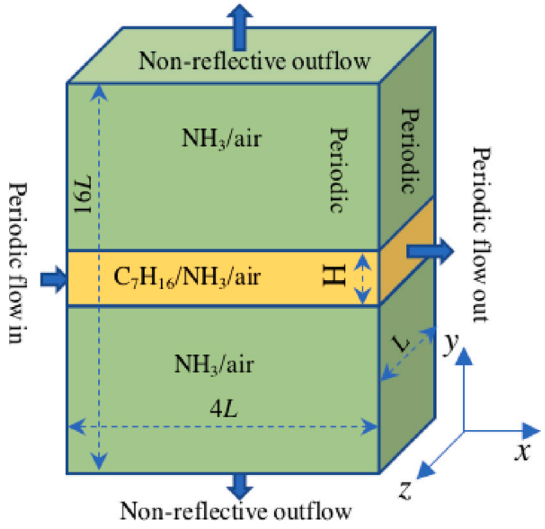

Fig. 1. A schematic of the DNS configuration. The origin of the x, y, z coordinate system is at the center of the domain, with the x, y, and z axes ranging from $[-2L, 2L]$, $[-8L, 8L]$, and $[-L/2, L/2]$, respectively.

the cross-flow (y-direction) boundaries to prevent pressure reflections from the domain edges and ensure accurate simulation of flow behavior inside the domain. The DNS configuration closely resembles the temporally evolving planar jet flames studied by Hawkes et al. [32,33], but it is applied here under high-pressure, high-temperature dual-fuel engine conditions. This setup was selected to efficiently capture the back-supported flame propagation while minimizing computational cost.

2.2. Domain initializations

The thermochemical states of the mixture are defined by the interaction between two streams: the n-heptane stream and the premixed ammonia/air stream. The premixed mixture stream is characterized by a temperature of 900 K and a pressure of 60 bar, conditions that replicate the in-cylinder state after the compression stroke. The equivalence ratio of the premixed ammonia/air mixture, ϕ_{NH_3}, varies from 0.3 to 0.9, allowing for the study of different fuel-air mixture compositions.

The n-heptane stream originates from liquid n-heptane at 300 K. To simulate diesel spray conditions, the liquid n-heptane stream undergoes adiabatic mixing with the premixed ammonia/air stream before the start of the DNS, following the methodology outlined by Krisman et al. [34] and Zhao et al. [31]. The evaporation of n-heptane is accounted for through this adiabatic mixing process. After mixing, the final central jet consists of a mass composition of 50% premixed ammonia/air and 50% n-heptane, with a resulting mixture temperature of 475 K.

The domain is initialized with isotropic and homogeneous turbulence, characterized by a turbulent velocity u' and an integral scale l_0. The premixed ammonia/air mixture has no mean flow, while the central jet is introduced with a velocity denoted as u_{jet}. Table 1 provides detailed values of u', l_0, and u_{jet}.

The mixing of the ambient mixture and center jet is characterized by the mixture fraction Z. It is defined as the normalized mass fraction of carbon, as described in Eq. (1):

$$Z = \frac{Y_C - Y_{C,min}}{Y_{C,max} - Y_{C,min}} \tag{1}$$

Here, $Y_C = Y_{C,min} = 0$ is set in the ambient ammonia/air mixture, while $Y_C = Y_{C,max}$ in the central jet. Based on this definition, the value of Z varies from 0 to 1.

The mixing layers are initialized between the central jet and the ambient gas. A hyperbolic tangent function is employed to initialize the mixture fraction Z within the mixing layer, as described in Eq. (2), where y indicates the vertical distance from the domain center,

$$Z = 0.5\,(1 + \tanh(5 - |y|/\delta)) \tag{2}$$

Here, the characteristic mixing length, or the thickness of the mixing layer, is set to be $\delta = H/10$.

The thermochemical states of the mixture, such as species mass fractions Y_i and temperature T, within the mixing layer, are determined as functions of Z. For Instance, the initial mass fraction of the ith species, Y_i is computed using the following relations:

$$Y_i = ZY_{f,i} + (1 - Z)Y_{a,i} \tag{3}$$

where the subscript i refers to the four species involved: NH_3, C_7H_{16}, N_2 (nitrogen), and O_2 (oxygen). The subscripts "f" and "a" correspond to the n-heptane and premixed ammonia/air streams, respectively. The initial temperature T within the mixing layer is similarly obtained.

2.3. DNS cases

Table 1 summarizes the numerical case setups, which include four one-dimensional (1D) cases and two three-dimensional (3D) cases. Two jet velocities (u_{jet}) are considered — 0 m/s (homogeneous turbulent flow without mean flow) and 10 m/s — to investigate the impact of jet velocity on RCCI combustion process. The equivalence ratio (ϕ_{NH_3}) of the premixed ammonia/air mixture ranges from 0.3 to 0.9 in the 1D cases. The 3D DNS studies focus on the $\phi_{NH_3} = 0.9$ condition, as it closely aligns with the ammonia/n-heptane RCCI engine experiments of Førby et al. [12], which demonstrated both high combustion efficiency and a high ammonia energy share.

The table also provides other important information, including velocity fluctuations (u_0'), domain width (L), ignition delay time (τ_{ig}), Reynolds number (Re_0), integral length scale (l_0), and Kolmogorov length scale (l_k).

Table 2 provides the mass fractions of species in the initial field, along with the laminar flame speed (s_L), laminar flame thickness (δ_L), and laminar flame time scale ($\tau_L = \delta_L/s_L$) of the premixed ammonia/air mixtures. These parameters are calculated under adiabatic planar flame conditions corresponding to the specified equivalence ratio, initial temperature, and pressure, using the same chemical kinetic mechanism and numerical solver as in the DNS. The equivalence ratios of the center n-heptane/ammonia/air mixtures range from 16 to 18.

The domain was discretized with a 10 μm mesh size, which is finer than the Kolmogorov scales (cf. Table 1). A mesh sensitivity test was performed on the 1D cases with $\phi_{NH_3} = 0.9$. The tested mesh sizes were 20, 10, 5, and 2.5 μm. Supplementary Materials S1 presents the spatial distribution of the mass fractions of NO and N_2O at several critical instances of time, the flame front position of the lean premixed flame, as well as the temperature and heat release rate ($\dot{Q}$) profiles at the lean premixed flame front at 3.5 ms. The results indicate that the species distribution and flame positions are well captured using the 10 μm mesh resolution.

2.4. DNS solver

The open-source computational fluid dynamics (CFD) software OpenFOAM is used in this study. The DNS solver, referred to as reactingDNS but with a specific implementation of transport properties, supports differential diffusion [35,36]. For spatial discretization, the finite volume method with a second-order scheme is employed, while the implicit second-order Crank–Nicolson scheme is utilized for time integration.

The detailed transport properties are calculated using the logarithm polynomial fitting method, and the mixture-average model is applied to compute the mixture transport properties. A skeletal ammonia/n-heptane reaction mechanism [37], consisting of 69 species and 389 reactions, is used to simulate the chemical reactions. This mechanism

Table 1
Case setup and key parameters. $Re_0 = u_0' l_0/(s_L \delta_L)$; $l_k = l_0/Re_0^{3/4}$. s_L and δ_L are laminar flame speed and flame thickness, respectively.

Case	ϕ_{NH_3}	u_0' (m/s)	u_{jet} (m/s)	L (mm)	δ/L	Re_0	l_0 (mm)	l_k (μm)	τ_{ig} (ms)
L03/05/07/09	0.3/0.5/0.7/0.9	–	–	1.28	0.1	0	–	–	0.89
H09	0.9	1.1	0	1.12	0.114	57	0.5	24	0.82
J09	0.9	1.1	10	1.12	0.114	57	0.5	24	0.98

Table 2
Key parameters of the central n-heptane stream and the ambient premixed ammonia/air stream in the 1D and 3D cases. $\tau_L = \delta_L/s_L$ is the time scale of the laminar premixed ammonia/air flame. $Y_{f,C_7H_{16}} = 0.5$ for all cases. For $\phi_{NH_3} = 0.3$ and 0.5 cases, the value of S_L is too low to achieve a reliable numerical solution.

ϕ_{NH_3}	s_L (m/s)	δ_L (μm)	τ_L (ms)	Y_{a,NH_3}	Y_{a,O_2}	Y_{a,N_2}	ϕ_f	Y_{f,NH_3}	Y_{f,O_2}	Y_{f,N_2}
0.3	–	–	–	0.048	0.224	0.729	16.0	0.024	0.112	0.365
0.5	–	–	–	0.077	0.217	0.706	16.7	0.038	0.109	0.353
0.7	0.163	53.8	0.331	0.104	0.210	0.686	17.4	0.052	0.105	0.343
0.9	0.237	40.6	0.171	0.130	0.204	0.666	18.1	0.065	0.102	0.333

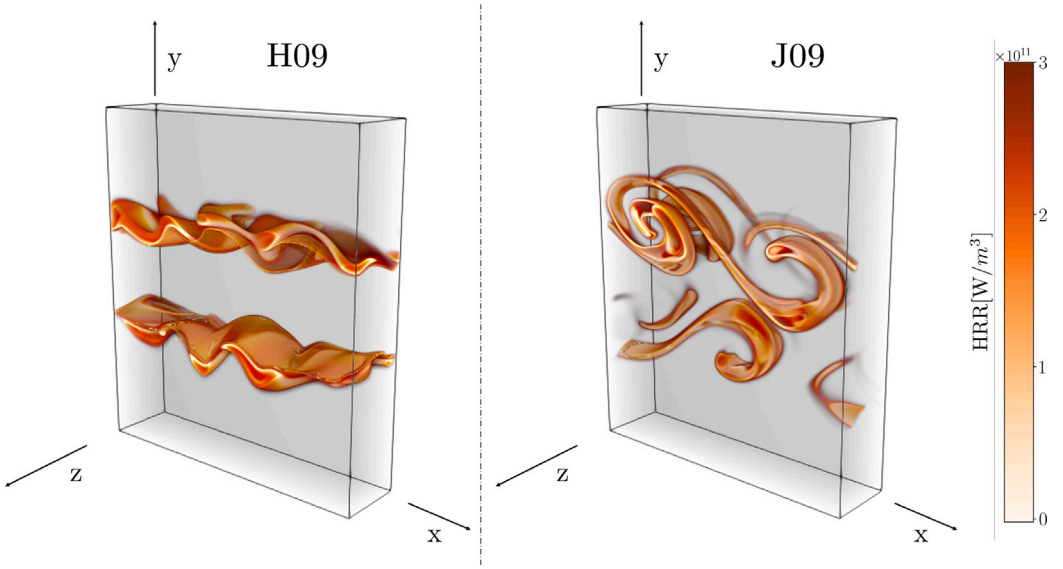

Fig. 2. 3D volumetric lighting of heat release rate in the mixing layer at $t = 0.9$ ms for Case H09 and $t = 1.0$ ms for Case J09.

has been extensively validated, demonstrating good agreement with experimental results for ignition delay time (IDT) and laminar flame speed across a range of relevant conditions.

The choice of OpenFOAM was primarily motivated by the need for flexibility, as the authors are also conducting combustion modeling research within the same framework. OpenFOAM offers a convenient platform for switching between tasks and integrating customized functionalities.

However, it should be acknowledged that OpenFOAM is limited to second-order numerical schemes, which necessitates fine mesh resolution in DNS. Alternative platforms such as S3D [38], the Pele Suite [39] (also based on a second-order scheme), NGA [40], and SOD2D [41] offer high-order numerical methods or adaptive mesh refinement (AMR), which can improve accuracy and efficiency.

3. Results and discussion

Fig. 2 presents a 3D visualization of the heat release rate (HRR) shortly after the onset of ignition for the two 3D cases. Here, $t = 0$ denotes the initial time of the simulation. For Case H09, thin heat release layers are observed, characterized by wrinkled planar structures. In contrast, for Case J09, the heat release zones are highly fragmented and concentrated in thin filamentary strips. The HRR distributions illustrate the different ways in which reactions progress between these two cases.

The results are sampled during the ignition process at a time instance when a significant temperature rise is observed in certain regions of the computational domain. To provide further insight, Figs. 3 and 4 show the distributions of temperature, HRR, and ammonia mass fraction for Cases H09 and J09 in the $z = 0$ cross-section at various instances of time.

Several observations can be made from Fig. 3. First, it is evident that the onset of ignition occurs in the mixing layer where large-scale vortices are formed; see $t = 0.8$ to 1 ms. The mixture in the premixed ammonia/air region exhibits low reactivity, making auto-ignition difficult. Similarly, the mixture in the center of the jet has a low temperature (475 K), which also hinders auto-ignition. Consequently, the onset of auto-ignition occurs in the mixing layer, where both temperature and reactivity are relatively high. Ignition is observed around $Z = 0.17$, where the local equivalence ratio (considering both ammonia and n-heptane fuels) is approximately 2.35.

Second, the HRR field at $t = 0.8$ to 1.2 ms shows the development of reaction zones, evolving from two layers to four layers. The two outer HRR layers propagate toward the premixed ammonia/air mixture, while the two inner HRR layers move toward the central n-heptane/ammonia/air mixture. Between the outer and inner HRR layers, the temperature is high (>2000 K), and ammonia is consumed, as observed at $t = 1.2$ ms.

Third, from $t = 1.4$ to 3.5 ms, it is evident that two new HRR layers form between the outer and inner HRR layers, resulting in six distinct thin HRR layers. The HRR in these two new layers is relatively low. During this time interval, the propagation of the outer HRR layers is relatively fast, while the inner HRR layers propagate more slowly. The

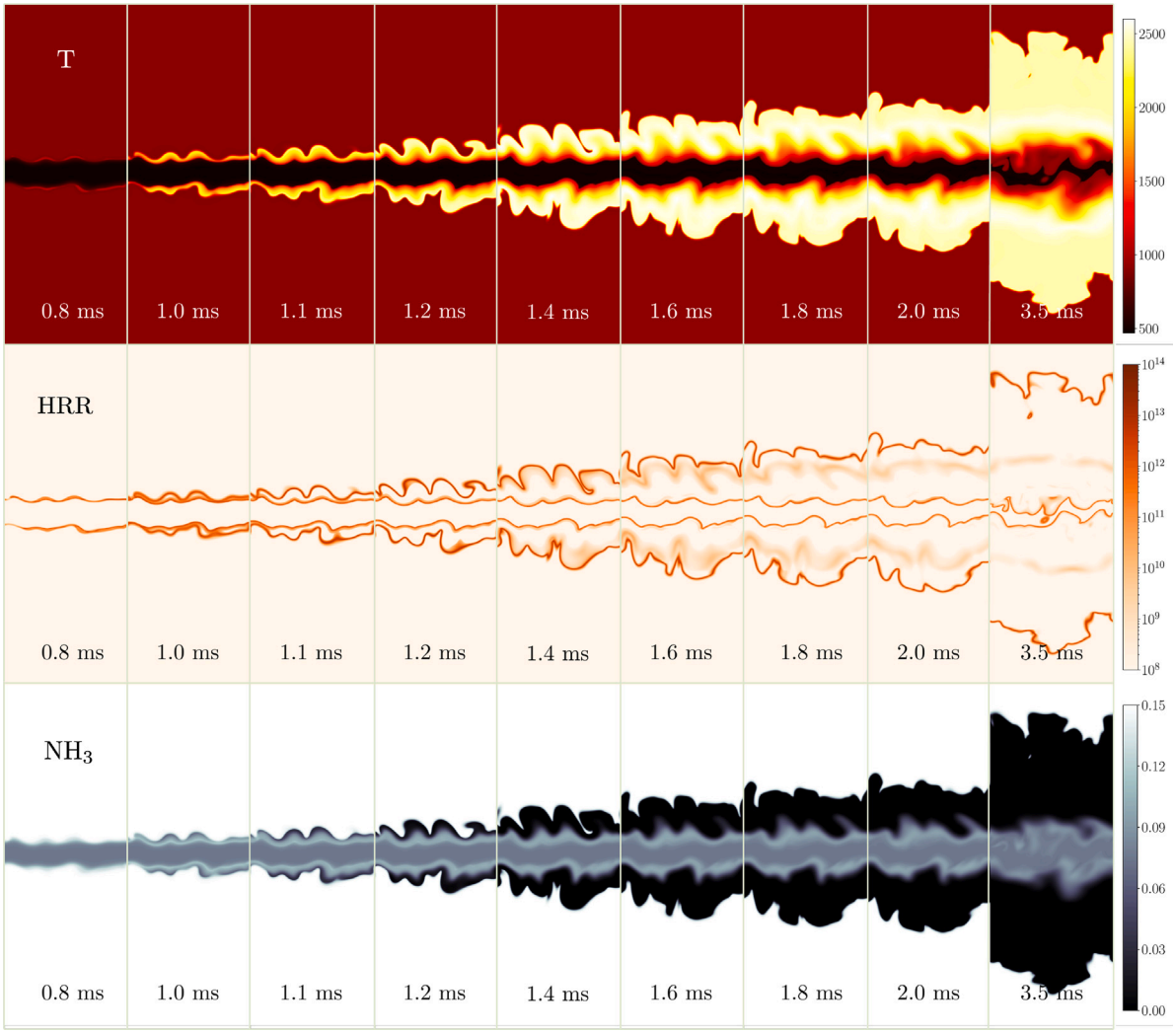

Fig. 3. Distribution of temperature, heat release rate (HRR), and ammonia mass fraction for Case H09 in the $z = 0$ cross-section at various time instances.

two new low-HRR layers propagate outward, following the outer HRR layers.

As the jet velocity increases to 10 m/s, large-scale vortex formation is observed, significantly affecting the ignition process and the structure of HRR zones, as shown in Fig. 4 for Case J09. The ignition delay time increases from 0.82 ms in the $u_{jet} = 0$ case to 0.98 ms in the $u_{jet} = 10$ m/s case. The ignition layer becomes more disturbed, transitioning from a wrinkled planar structure to highly twisted, thin filamentary strips, as illustrated in Figs. 2 and 4. From $t = 1.1$ ms to 1.7 ms, the ignition kernels propagate within the mixing layer toward both the lean and rich sides of the mixtures. At $t = 1.7$ ms, six HRR layers can be observed, with the inner HRR layers beginning to merge. By $t = 2.5$ ms, the two inner HRR layers have already merged and disappeared after the complete consumption of oxygen in the center fuel-rich region, leaving four HRR layers remaining.

The ignition process, reaction layer structures, combustion modes, and emissions of NO and N_2O are analyzed in greater detail below.

3.1. Ignition process

The ignition in both cases initially occurs within the mixing layer, where the combination of temperature and reactivity promotes the onset of chemical reactions. Chemical reaction pathway analysis, based on the employed mechanism [37], reveals that the n-heptane/ammonia/air mixture in the mixing layer first undergoes low-temperature ignition via the reaction sequence $C_7H_{16} \rightarrow C_7H_{15} \rightarrow C_7H_{15}O_2 \rightarrow C_7H_{14}OOH \rightarrow OH$; this pathway results in the formation of OH radicals, which subsequently react with fuels and combustion intermediates, leading to a modest amount of heat release and a corresponding temperature increase of approximately 100 K. This phenomenon, referred to in the literature as the cool flame, is primarily responsible for the negative-temperature coefficient (NTC) behavior observed in n-heptane ignition under intermediate temperature conditions, typically in the range of 700–900 K [42,43].

The effect of ammonia mass fraction in the ambient premixed ammonia/air mixture on ignition in the mixing layer has been investigated in the 1D cases (L03 - L09). Under the current RCCI conditions, it is observed that the onset of cool flame or low-temperature ignition occurs within a time frame of 0.38 ms (for $\phi_{NH_3} = 0.3$) to 0.75 ms (for $\phi_{NH_3} = 0.9$); this variation is attributed to the increased ammonia mass fraction in the ambient premixed ammonia/air mixture, which delays low-temperature reactions due to competing reactions where ammonia reacts with OH radicals, thus reducing the availability of OH for n-heptane-related chemistry. A similar phenomenon has been reported in the literature [18,20,21]. More results and figures about the 1D cases are presented in Supplementary Materials S2 (Fig. S4).

Following the completion of the low-temperature ignition process, the system transitions into the high-temperature reaction regime, characterized by the formation of hydrogen peroxide (H_2O_2) and subsequently an accelerated production of hydroxyl radicals (OH), leading to rapid heat release and a significant temperature rise.

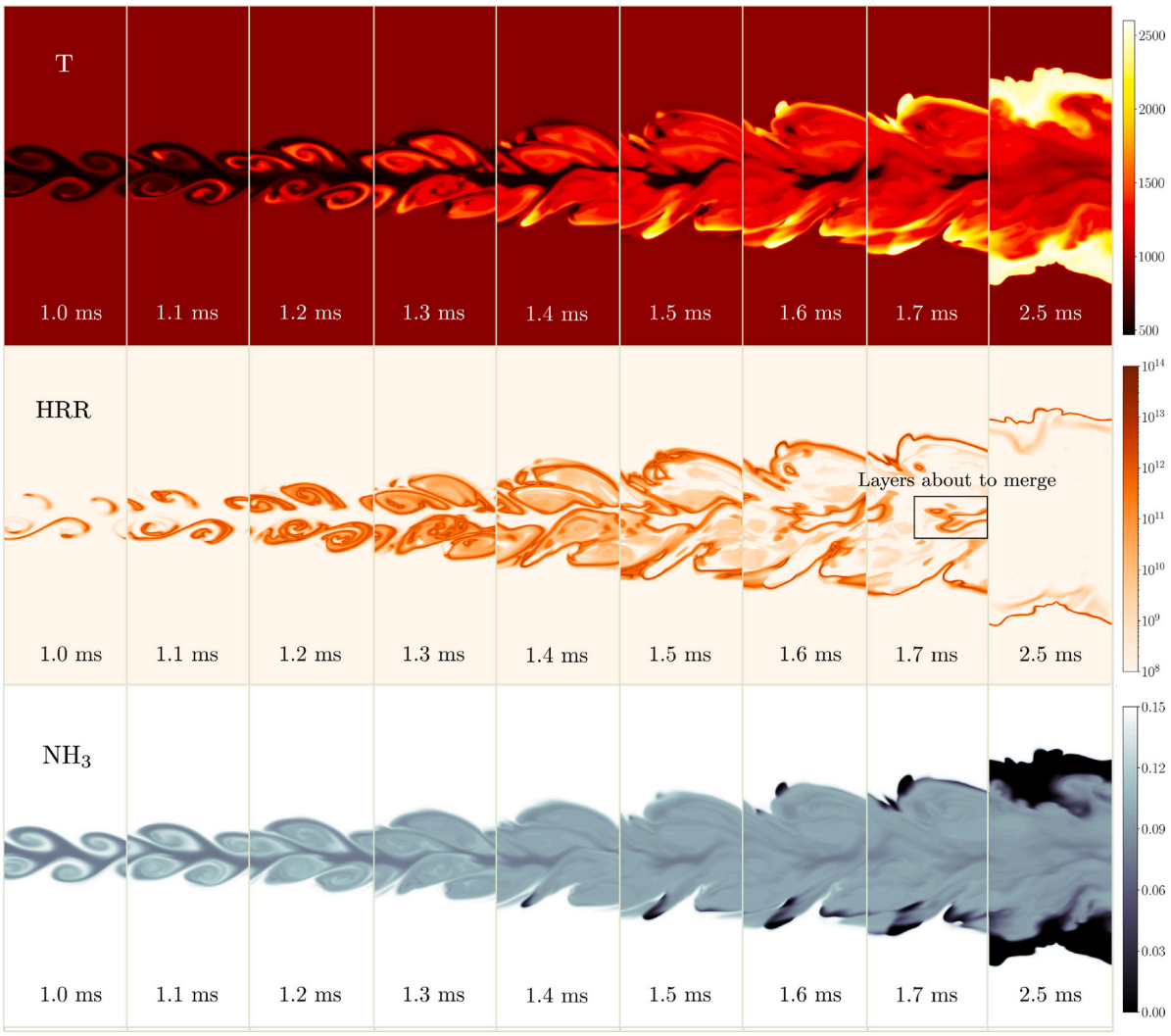

Fig. 4. Distribution of temperature, heat release rate (HRR), and ammonia mass fraction for Case J09 in the $z = 0$ cross-section at various time instances.

It is found that during the low-temperature ignition phase, the OH mass fraction reaches approximately 10^{-5}; in contrast, during the high-temperature ignition stage, this value increases substantially to about 2×10^{-3}. The ignition delay time, as commonly defined, corresponds to the point at which 2% of the maximum OH intensity is reached [44] in OH-PLIF measurements. Under the present conditions, this criterion roughly corresponds to the moment when the temperature at the ignition site rises to 1500 K, at which point the OH mass fraction is approximately 2% of its maximum value (cf. Fig. S4 and the relevant text in Supplementary Materials S2). Consequently, the time required for the temperature to reach 1500 K has been adopted in this study as the metric for defining the ignition delay time. Using this definition, the onset of ignition occurs at approximately 0.82 ms and 0.98 ms for Cases H09 and J09, respectively; see Table 1. This demonstrates the impact of jet velocity on the ignition process.

Figs. 5 and 6 present the scatter plot of the mixtures in the mixing layer in the $\phi - \chi$ coordinates for the two 3D cases, where χ is the scalar dissipation rate. Each dot in the figure represents a point in the mixing layer. Since multiple points can share the same values of ϕ and χ but exhibit different reaction progress, the maximum values of heptyl-peroxide mass fraction ($Y_{C_7H_{15}O_2}$) or temperature at a given ϕ and χ are shown using the color bars. The scalar dissipation rate, χ, is defined as:

$$\chi = 2D\nabla Z \cdot \nabla Z \tag{4}$$

where D is the mass diffusion coefficient of the mixture. χ represents the mixing rate between the cold n-heptane jet and the surrounding hot premixed ammonia/air mixture.

For the $u_{jet} = 0$ case (H09), shown in Fig. 5, it is observed that low-temperature reactions occur at $t = 0.7$ ms, primarily around $\phi \sim 2 - 3$ and at low χ values ($\chi \sim 0 - 75$ 1/s), as indicated by the presence of $C_7H_{15}O_2$. At this stage, the temperature remains low. By $t = 0.8$ ms, $C_7H_{15}O_2$ has spread to richer mixtures with $\phi \sim 2 - 4$ and higher χ values, up to $\chi \sim 0 - 200$ 1/s. Around $\phi \sim 2.5$ and $\chi < 10$ 1/s, $C_7H_{15}O_2$ is consumed, leading to a temperature rise approaching 1500 K. At $t = 0.82$ ms, this location reaches high-temperature ignition, with the local temperature reaching 1500 K (this figure is omitted for brevity). In summary, ignition in the mixing layer occurs at low scalar dissipation rates, with the most favorable ϕ value being approximately 2.5.

For the $u_{jet} = 10$ m/s case (J09), shown in Fig. 6, low-temperature reactions occur similarly at $t = 0.7$ ms, around $\phi \sim 2 - 3$ and at low χ values ($\chi \sim 0 - 200$ 1/s). By $t = 0.8$ ms, the low-temperature reactions spread to much richer mixtures and higher χ values; however, the maximum temperature in the mixing layer remains below 1200 K, and high-temperature ignition has not yet occurred. This indicates a longer interval between the onset of low-temperature reactions and high-temperature ignition for the $u_{jet} = 10$ m/s case compared to the $u_{jet} = 0$ case. At $t = 1$ ms, the onset of high-temperature ignition is observed, as shown in Fig. 6, occurring around $\phi \sim 3 - 4$ and $\chi < 100$ 1/s, slightly richer than the low jet velocity case. At this time, however,

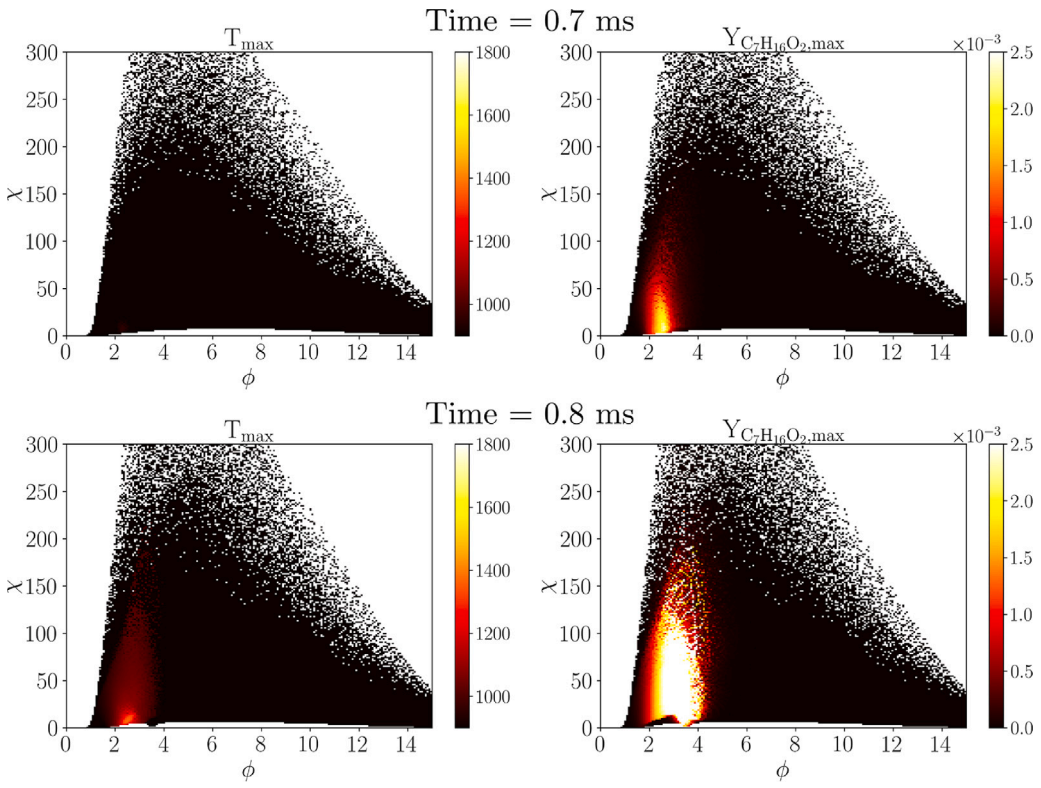

Fig. 5. Scatter plots of the maximum T and $Y_{C_7H_{15}O_2}$ in the mixing layer in the equivalence ratio (ϕ) and scalar dissipation rate (χ) coordinates for Case H09 at two time instances around the onset of ignition. (For interpretation of the references to color in this figure legend, the reader is referred to the web version of this article.)

the cool flame has spread across most of the $\chi - \phi$ space, highlighting the impact of jet velocity on the ignition process.

Fig. 7 shows the two-dimensional distribution of temperature, scalar dissipation rate, and mass fractions of OH and $C_7H_{15}O_2$ in the z = 0 cross-section at four time instances during the ignition process of Case J09, revealing the impact of jet-induced vortices on the ignition process. The onset of ignition is shown to be closely connected to the formation of vortices in the mixing layer. The ambient hot ammonia/air mixture is entrained by the vortex into the n-heptane jet core region. Within the vortex core, the scalar dissipation rate is low, which favors ignition reactions [45].

At t = 1.0 ms, the vortex core, as shown in the zoomed region, exhibits a high mass fraction of $C_7H_{15}O_2$, accompanied by a small amount of OH radicals and a mild temperature rise. By t = 1.1 ms, this same vortex core undergoes high-temperature ignition, with $C_7H_{15}O_2$ being consumed to form a high concentration of OH radicals and a rise in temperature, indicating a transition from a low-temperature ignition core to a high-temperature ignition core. At the edge of this ignition core, a thin layer of $C_7H_{15}O_2$ is observed, representing the cool flame front propagating into the remaining vortex region, as shown at t = 1.2 ms. The OH layer follows the $C_7H_{15}O_2$ layer, indicating subsequent high-temperature ignition front propagation.

This process continues until the reaction front propagates into the ambient premixed ammonia/air mixture, with the remaining jet region being partially oxidized by the cool flames. Vortex roll-up significantly enhances the propagation of the ignition front, as also shown in Figs. 3 and 4.

In summary, the ignition in the studied ammonia/n-heptane RCCI combustion cases occurs first in the mixing layer, and the most favorable equivalence ratio lies between 2 and 4. The mixing layer vortices play a crucial role in the ignition process, with ignition occurring at the vortex core, where the local scalar dissipation rate is minimal. The ignition core exhibits a temporal evolution, initially undergoing low-temperature ignition, followed by high-temperature ignition.

The following section investigates the combustion modes and reaction zone structures during the late RCCI combustion stage after the onset of ignition.

3.2. Reaction layers and combustion modes in the later stage of RCCI combustion

Fig. 8 shows the spatial distributions of HRR, temperature, and mass fractions of key species in the z = 0 cross-section for Case H09 at t = 3.5 ms, illustrating the reaction zone structures and combustion modes in the later stage of RCCI combustion. As discussed earlier, in the later stage of RCCI combustion, six HRR layers can be identified, corresponding to three combustion modes: lean premixed flame (LPF), rich premixed flame (RPF), and diffusion flame (DF). The LPF corresponds to the outer HRR layers, propagates into the premixed ammonia/air mixture, and consumes ammonia while forming NO. The RPF corresponds to the low-temperature ignition of n-heptane, also known as the cool flame [35,42,43,46]. This process is associated with a slight increase in temperature and a small amount of heat release, as shown in Fig. 8.

The DF coincides with the isoline of the equivalence ratio of one, i.e., around the stoichiometric mixture. It separates the fuel-lean mixture from the fuel-rich mixture, where oxidizers (such as remaining O_2 and radicals like OH) in the post-flame zone of the LPF diffuse to the DF and react with the unburned fuels and combustion intermediates (such as H_2) diffused from the fuel-rich mixture. In the DF, NO formed in the LPF reacts with combustion intermediates such as imidogen radicals (NH), nitrogen radicals (N), and hydrogen (H_2) from the fuel-rich mixture. Notably, NO is nearly completely consumed in the DF.

The fuel-rich mixture between the DF and RPF contains an additional reaction layer where ammonia undergoes oxidation, forming intermediate species such as H_2. This layer is referred to as the rich ammonia oxidation layer (RAOL). In this reaction layer, there is no significant heat release. Between RAOL and RPF, there is a layer where

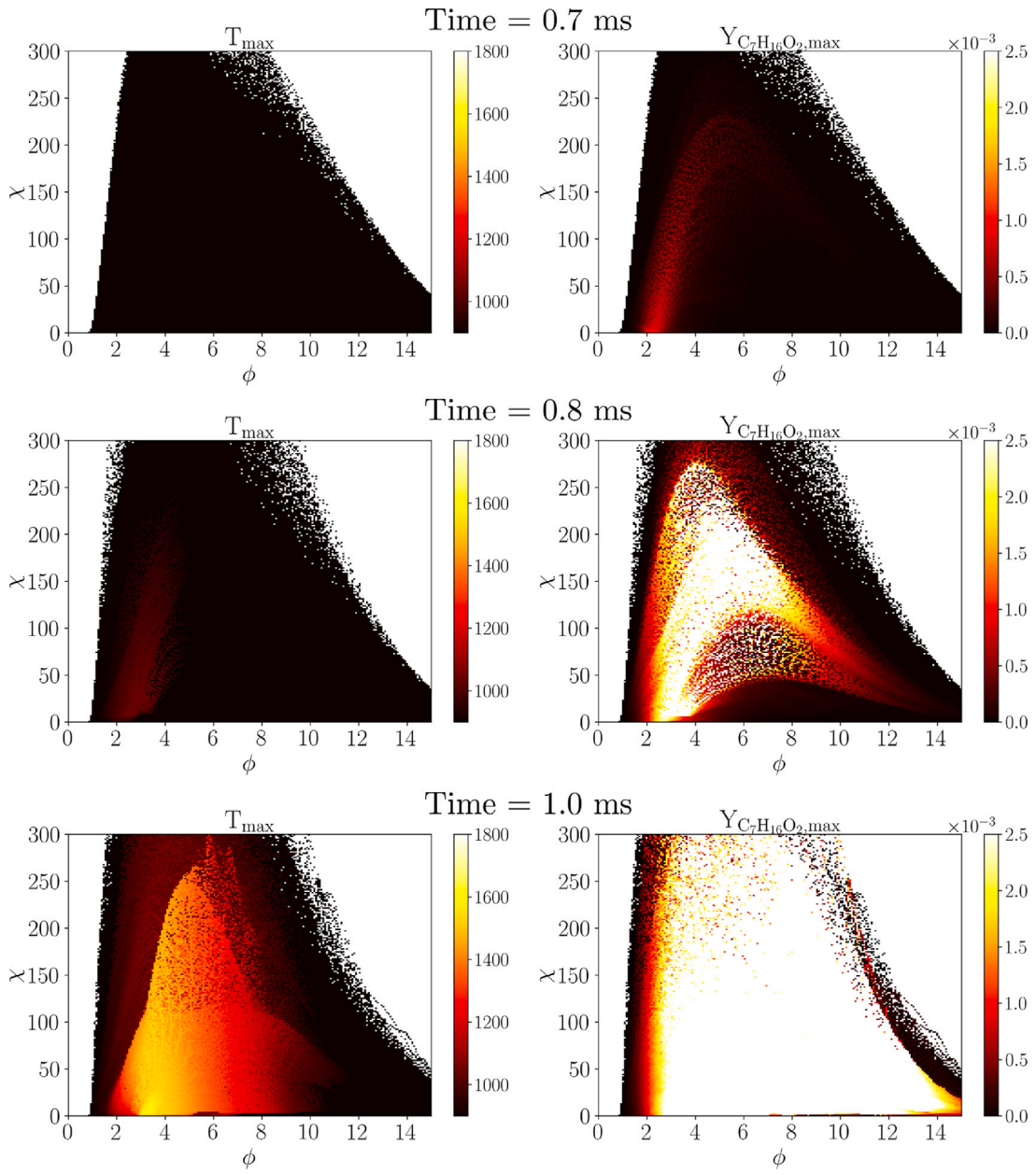

Fig. 6. Scatter plots of the maximum T and $Y_{C_7H_{15}O_2}$ in the mixing layer in the equivalence ratio (ϕ) and scalar dissipation rate (χ) coordinates for Case J09 at three time instances around the onset of ignition. (For interpretation of the references to color in this figure legend, the reader is referred to the web version of this article.)

NO and N_2O are notably distributed. This layer is identified by the red isoline of $Y_{C_7H_{16}} = 0.12$, indicating that the fuel is only partially oxidized.

To further investigate NO and N_2O formation and consumption in the DF and RPF, several relevant species along the line $x = 0$ in the $z = 0$ plane for Case H09 at $t = 3.5$ ms are shown in Fig. 9a. The NO/N_2O reaction rates along this line are shown in Supplementary Materials S3, Fig. S5. In the RPF, the temperature is lower than 1500 K. The low-temperature reaction of n-heptane involves the formation and consumption of $C_7H_{15}O_2$, leading to a moderate temperature rise. NO is primarily formed through the reaction $H + NO_2 \rightarrow NO + OH$ in the RPF and the adjacent region, where local peaks of NO and N_2O are observed. Once produced, NO is consumed via reaction $NO + HO_2 \rightarrow OH + NO_2$, forming nitrogen dioxide (NO_2). In the same region, N_2O is generated through the reaction $NO_2 + NH_2 \rightarrow N_2O + H_2O$ and is subsequently consumed in the reaction $H + N_2O \rightarrow OH + N_2$. In the RAOL, the above-discussed reactions reach partial equilibrium, resulting in low concentrations of NO and N_2O.

In the DF, NO produced at the LPF is consumed through the reactions $NO + N \rightarrow N_2 + O$, $NO + H_2 \rightarrow HNO + H$, and $NO + NH \rightarrow N_2O + H$. The species N, NH, amidogen radical (NH_2), and H_2 originate from the oxidation of NH_3 in the RAOL. As for N_2O, its formation and consumption reactions balance each other in the DF, leading to a partial equilibrium state in which N_2O remains at a low concentration.

The impact of jet velocity on the flame structures and combustion modes is visualized in Fig. 10. Notably, at $t = 3.5$ ms, the RPF has disappeared, leaving only the LPF, DF, and RAOL remaining in the domain. The jet-induced large-scale vortices and turbulence significantly enhance the mixing of the fuel-rich mixture with the fuel-lean mixture, causing the DF location to shift further into the fuel-lean mixture compared to Case H09. The RPF propagates much faster, and eventually, the two RPF layers merge with each other and disappear from the domain. The propagation of the LPF is less significantly affected by the jet since the LPF is far away from the jet mixing layer. However, due to the faster propagation of the DF, the LPF and DF are

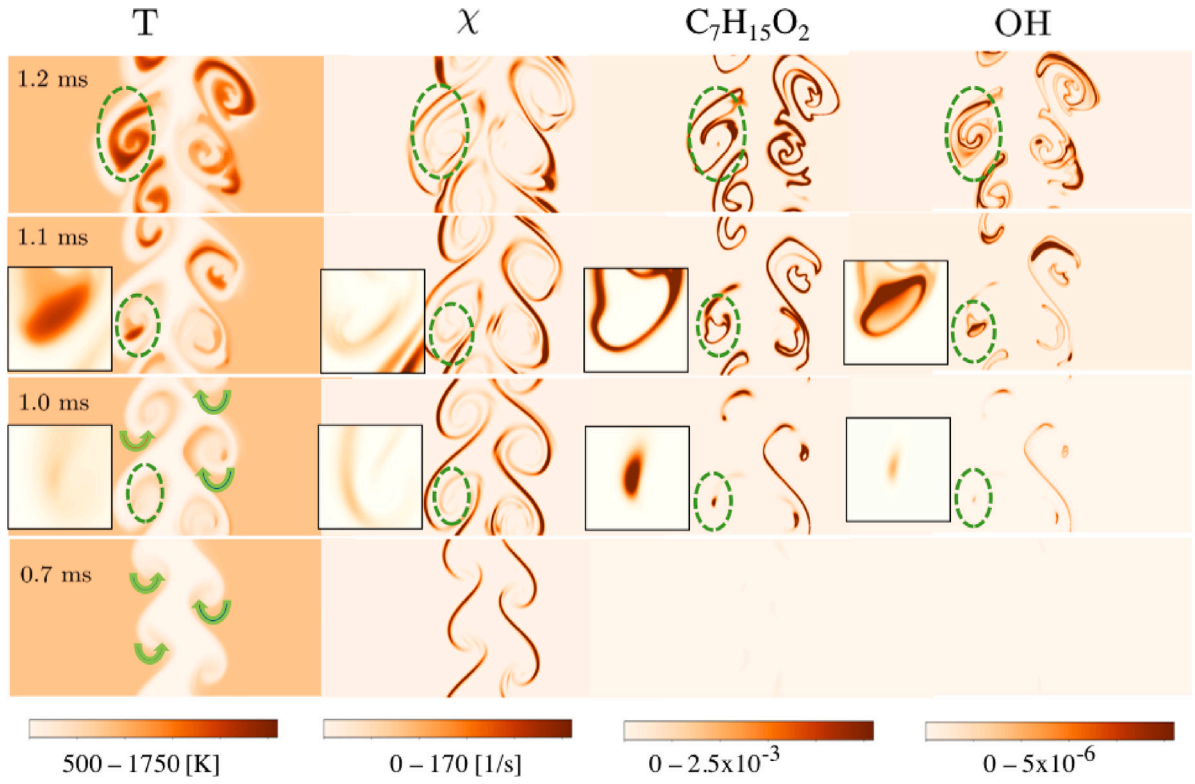

Fig. 7. Temporal evolution of the temperature (T), scalar dissipation rate (χ), mass fractions of $C_7H_{15}O_2$ and OH in the $z = 0$ cross-section during the ignition process for Case J09. A magnified box region highlights the ignition kernel.

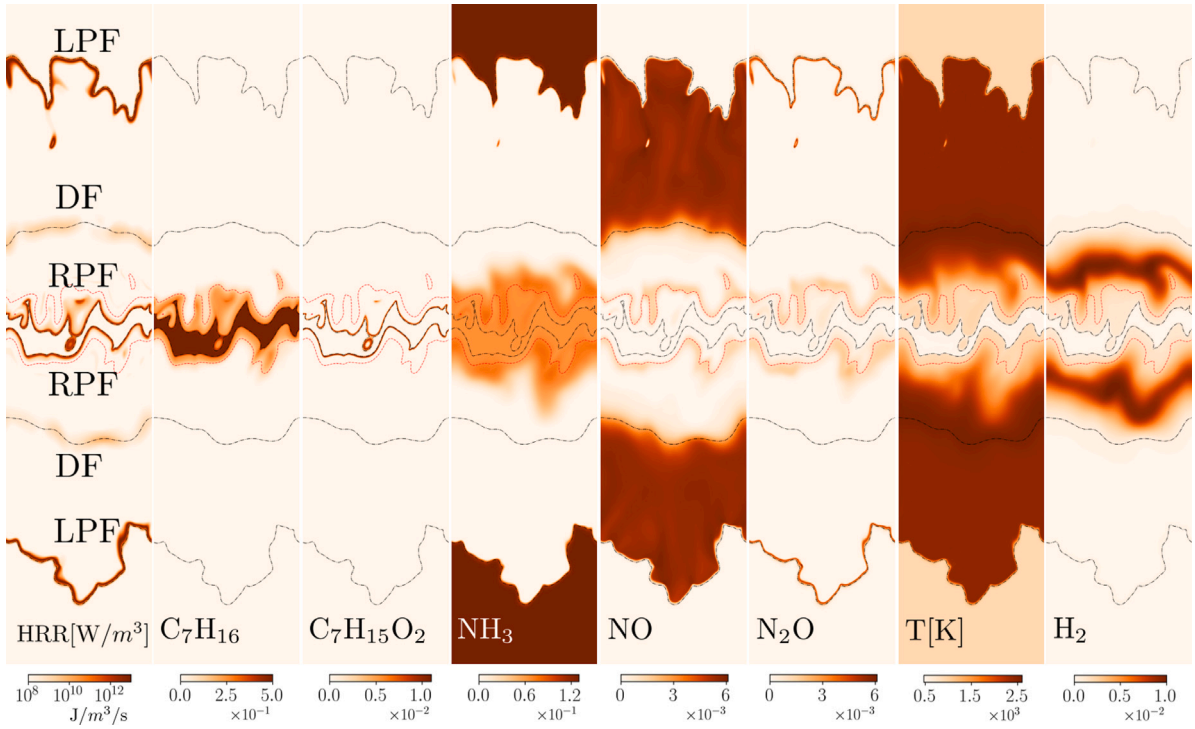

Fig. 8. Distribution of HRR and species mass fractions at $t = 3.5$ ms for Case H09. HRR layers are marked with black dashed lines in species fields. $Y_{C_7H_{16}} = 0.12$ contours, which mark layers with NO and N_2O formation near RPF, are colored in red for reference. (For interpretation of the references to color in this figure legend, the reader is referred to the web version of this article.)

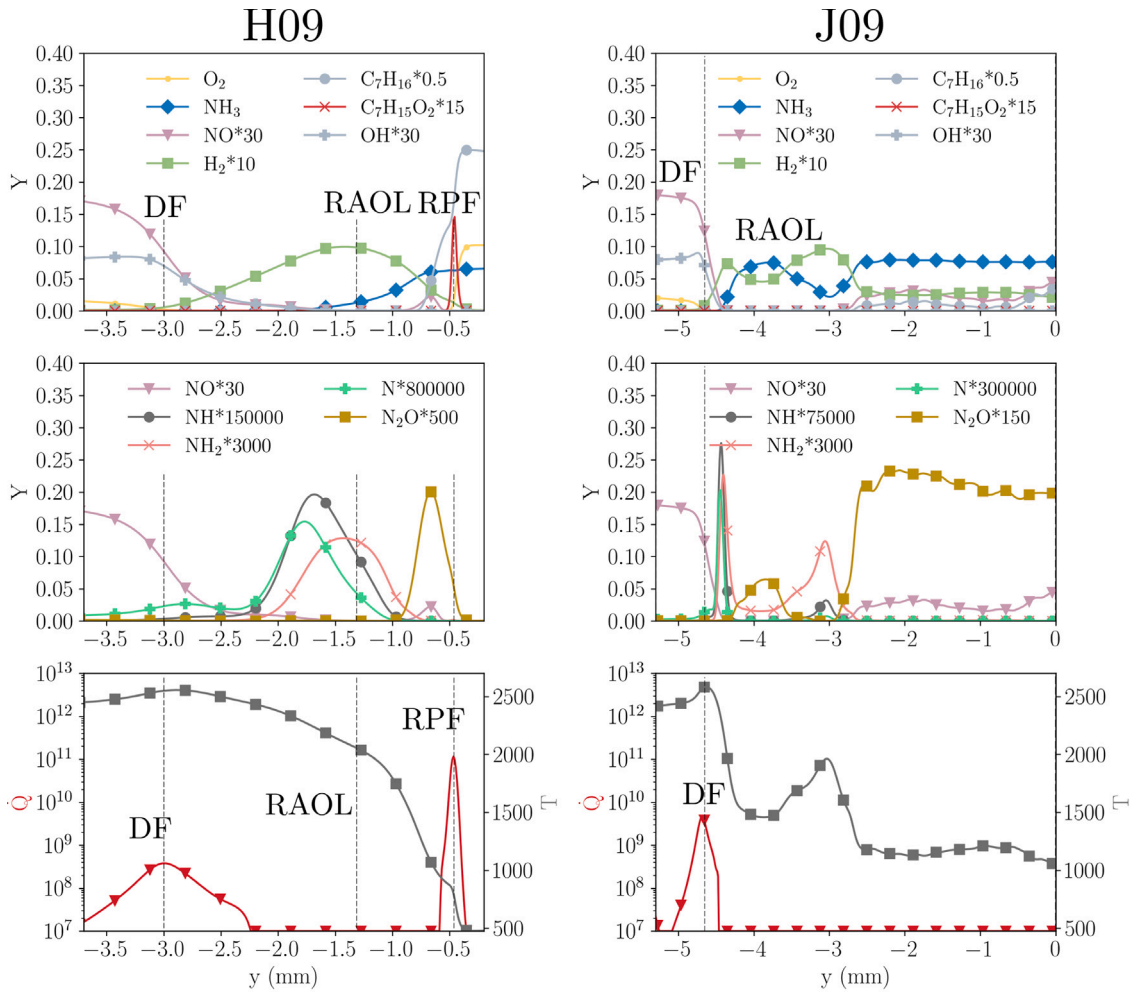

Fig. 9. Distribution of heat release rate (HRR) and species mass fractions at $t = 3.5$ ms along the line $x = 0$ and $z = 0$ for Cases H09 (a) and J09 (b).

located much closer to each other. Consequently, the high-NO region is smaller, as the jet enhances NO consumption reactions.

In the fuel-rich zone (between the two DF layers), a significantly higher concentration of N_2O is observed compared to the no-jet case (H09) at $t = 3.5$ ms. The formation of N_2O in this region originates from the cool flames at earlier times, through the reaction $NO_2 + NH_2 \rightarrow N_2O + H_2O$, while its consumption is negligible, cf. Figs. S7 and S8 in Supplementary Materials S4. The N_2O formation reaction is enhanced when more NH_3 is entrained into the n-heptane region, resulting in a higher accumulation of N_2O in the domain. At $t = 3.5$ ms, as shown in Figs. 9b, 10, and Fig. S6, the temperature in this region remains relatively low, and there is insufficient oxygen around. Consequently, the mixture is nearly chemically frozen, preventing the further consumption of N_2O, leading to its sustained high concentration in the later stages.

It should be noted that the pathway analysis presented here may be specific to the chemical kinetics model employed in this study [37]. Numerical studies using other chemical kinetics models, such as those developed by Alekseev et al. [47] and Wang et al. [48], exhibit similar overall trends in the simulations for case L09, although variations in quantitative results and the details of individual elementary reactions do exist. These discrepancies do not affect the conclusions drawn in this study. Additional discussion can be found in the final section of the Supplementary Materials.

3.3. Propagation of LPF

The back-support of n-heptane on the propagation of the LPF front is analyzed. The displacement speed of the LPF, defined at the iso-surface of the reaction progress variable $c = 1 - Y_{O_2}/Y_{a,O_2} = 0.5$, is used to characterize the propagation of the LPF, where Y_{a,O_2} is the mass fraction of O_2 in the ambient mixture, cf. Table 2:

$$S_d = \frac{\partial Y_{O_2}/\partial t + \boldsymbol{u} \cdot \nabla Y_{O_2}}{|\nabla Y_{O_2}|} \tag{5}$$

where $\boldsymbol{u}$ is the velocity vector at the iso-surface $c = 0.5$. For comparison with the corresponding laminar flame speed of a 1D freely propagating flame, S_d is normalized with the density ratio ρ/ρ_u,

$$S_L = \frac{\rho}{\rho_u} S_d \tag{6}$$

where ρ is the density at the iso-surface $c = 0.5$, and ρ_u is the density of the unburned premixed ammonia/air mixture.

Fig. 11 shows the joint probability density function (JPDF) of S_L and Z at different time instances after ignition. The value of Z at the LPF front decreases with time as the LPF propagates into the ambient ammonia/air mixture. The mean value of S_L ($\bar{S}_L$) decreases as Z decreases. When $Z < 10^{-4}$, $\bar{S}_L$ approaches the laminar flame speed of the ambient premixed ammonia/air mixture ($S_{L,0}$), indicating the termination of the back-support effects. These back-support effects are limited to a short period of time—approximately 2 ms for Case H09

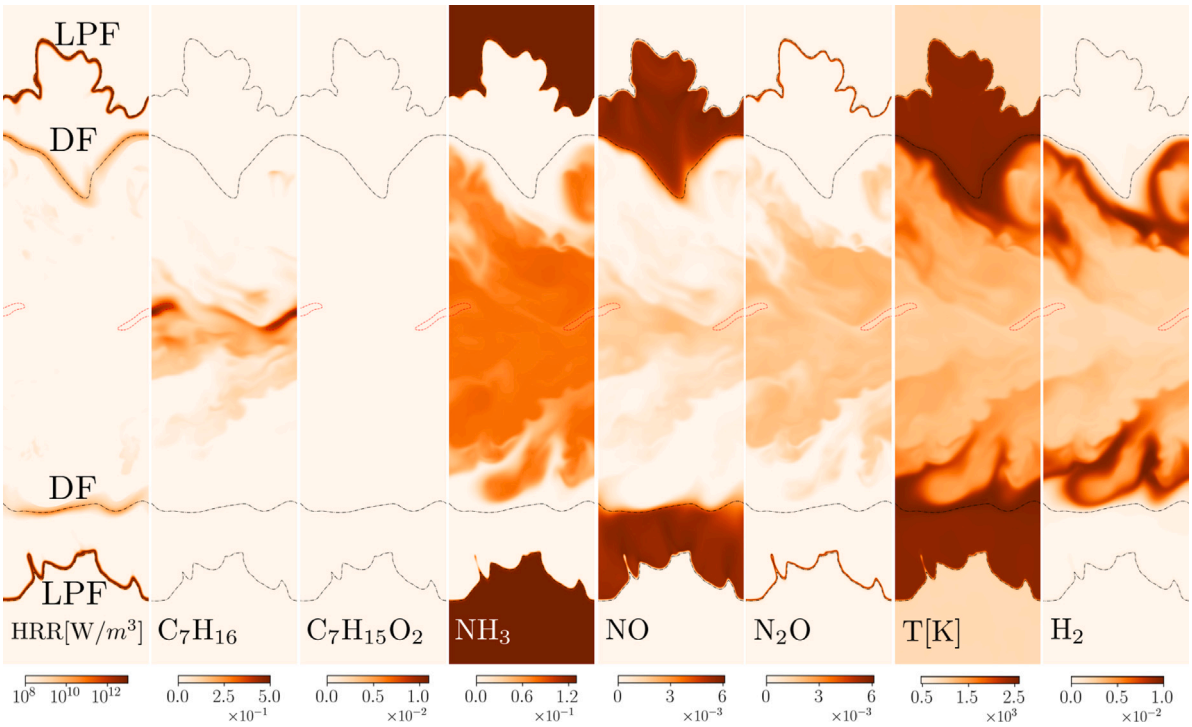

Fig. 10. Distribution of HRR and species mass fractions at $t = 3.5$ ms for Case J09. HRR layers are marked with black dashed lines in species fields. $Y_{C_7H_{16}} = 0.12$ contours, which mark layers with NO and N_2O formation near RPF, are colored in red for reference. (For interpretation of the references to color in this figure legend, the reader is referred to the web version of this article.)

and 3 ms for Case J09. Compared to the $u_{jet} = 0$ case (H09), the $u_{jet} = 10$ m/s case (J09) exhibits a longer duration of back-support due to enhanced heat and mass transfer in the mixing layer and the wider spread of the mixing layer in the cross-flow y-direction. This is also evident in the faster spread of the DF in the y-direction for Case J09, as shown in Figs. 3 and 4.

The n-heptane stream influences LPF propagation through three physical and chemical mechanisms: (a) the mixing of the highly reactive fuel, n-heptane, into the ammonia/air mixture, (b) the supply of heat, radicals, and intermediate species from the combustion in the DF, and (c) the enhanced turbulent mixing due to jet-induced turbulence and large-scale vortices in the mixing layer.

Before the onset of high-temperature ignition, n-heptane in the central jet region is transported by turbulence into the ambient ammonia/air mixture, contributing to the first mechanism. A longer ignition delay in Case J09 results in increased mixing of n-heptane into the ambient mixture. After ignition and the formation of the LPF, RPF, and DF fronts (e.g., $t > 1$ ms for Case H09 and $t > 1.2$ ms for Case J09; cf. Figs. 3 and 4), the second mechanism comes into effect. The heat, radicals, and combustion intermediates are transported to the reaction zone of the LPF, enhancing reactions and thus accelerating flame propagation. Additionally, turbulence and large-scale vortices in the mixing layer—the third mechanism—enhance the mixing of n-heptane with the ambient mixture and the transport of hot combustion intermediates and radicals to the LPF, further influencing its propagation speed. This is also the reason for the faster propagation of DF toward LPF discussed earlier and the longer back-support time of the J09 case.

The impact of the three mechanisms may be understood by comparing the mean value of S_L and the corresponding values of S_L in the 1D Case L09 ($S_{L,1}$) and the 1D freely propagating flame results with given Z values ($S_{L,0}$). In the latter case, the initial mixture and temperature were set according to those in the mixing layer at specific values of Z. For both H09 and J09 cases, it is seen that $\bar{S}_L > S_{L,1} > S_{L,0}$. $\Delta S_{L,1} = S_{L,1} - S_{L,0}$ is attributed to the second mechanism, while $\Delta S_{L,2} = \bar{S}_L - S_{L,1}$ reflects the impact of the third mechanism. One may examine the relative impact of the three mechanisms by comparing $\Delta S_{L,1/2}$ with $S_{L,0}$.

It is clear that $\Delta S_{L,2}$ and $\Delta S_{L,1}$ are smaller than $S_{L,0}$, indicating that the first mechanism—the mixing of n-heptane into the ambient ammonia/air mixture before the onset of ignition—is the dominant mechanism enhancing LPF propagation in the earlier stage of the LPF propagation process.

The value of S_L varies over a wide range at a given Z, owing to the local flame curvature and strain rate. Fig. 12 shows the scatter plots of S_L and curvature evaluated at the LPF fronts at $t = 3.5$ ms. For both flames, S_L is closely correlated with the curvature of the LPF front. When the wrinkled flame front is convex toward the burned side (negative curvature), the reaction zone of the LPF experiences increased heating, an enhanced concentration of radicals (e.g., OH), an enhanced heat release rate, and thereby an increased local displacement speed, S_L. Conversely, when the wrinkled flame front is convex toward the unburned side (positive curvature), the local heat release rate and local displacement speed are suppressed. Similar effects of curvature on the HRR for ammonia/air premixed flames at atmospheric pressure have been reported by Yang et al. [49].

3.4. *Emission characteristics of* NO *and* N_2O

Fig. 13 shows the temporal evolution of the normalized total HRR and the total masses of NO and N_2O in the domain. Based on the results in Sections 3.1 and 3.3, four stages can be identified to describe the combustion and emission process: stage 1—the mixing stage before the onset of ignition; stage 2—the ignition stage, characterized by a rapid increase in HRR over time; stage 3—the back-supported flame propagation stage, characterized by a decreasing HRR over time; and stage 4—the LPF propagation stage.

Taking Case H09 as an example, a rapid increase in HRR is observed in Stage 2, starting around 0.8 ms, which is about the IDT of this case. The HRR peaks at approximately 1.2 ms, coinciding with the formation of four reaction layers: LPF and RPF (cf. Fig. 3). From

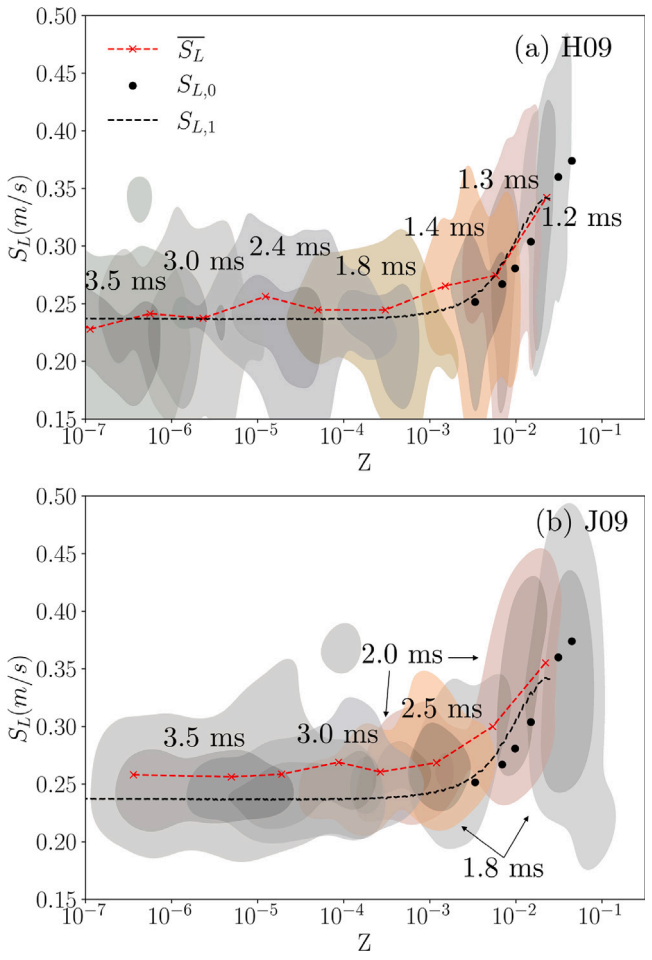

Fig. 11. JPDF of Z and S_L at representative time instances for Cases (a) H09, and (b) J09. The red line ($\bar{S}_L$) represents the corresponding mean value of S_L at a given Z. The dashed line ($S_{L,1}$) represents the corresponding values of S_L at a given Z for Case L09. The solid circles ($S_{L,0}$) indicate the laminar flame speed of 1D planar freely propagating flames in n-heptane/ammonia/air mixtures at the given Z. Each JPDF plot includes two contour levels: the outer contour encompasses 80% of the simulation data, while the inner contour covers 40%. (For interpretation of the references to color in this figure legend, the reader is referred to the web version of this article.)

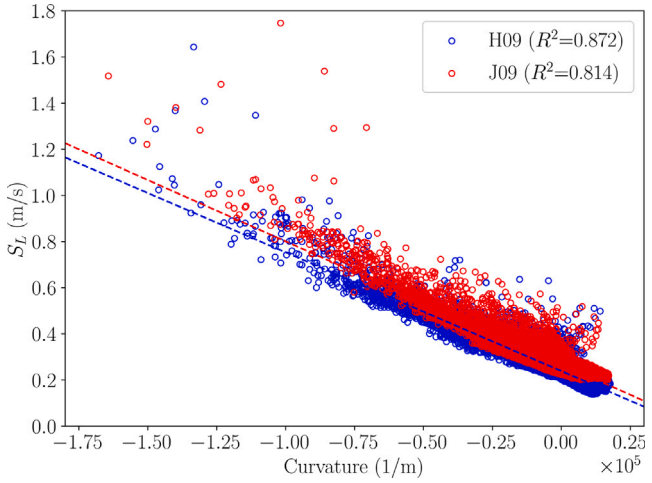

Fig. 12. Scatter plot of S_L and curvature at $t = 3.5$ ms for Cases H09 and J09.

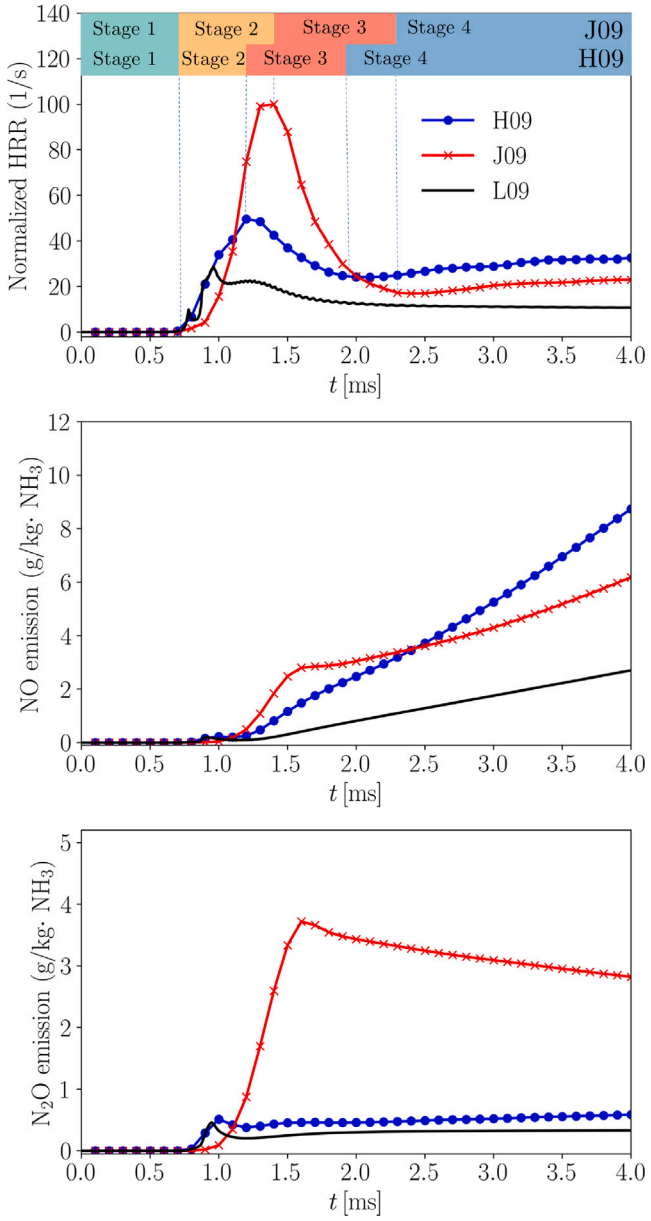

Fig. 13. Temporal evolution of (a) total heat release rate (HRR), (b) total mass of NO, and (c) total mass of N_2O in the domain. The total HRR is normalized by the initial total energy of the fuels in the domain, while the NO and N_2O emissions are normalized by the initial mass of NH_3 in the domain.

1.2 ms to 2 ms, the HRR decreases over time due to the diminishing influence of n-heptane on the back-supported flame propagation in Stage 3, as discussed in the previous section. After 2 ms, in Stage 4, the unsupported LPF propagates through the ambient ammonia/air mixture at a relatively constant speed, resulting in a nearly constant HRR.

After 1.2 ms, in Stages 3 and 4, the mass of NO in the domain increases monotonically as the LPF propagates into the ambient ammonia/air mixture. As shown in Fig. 8, NO is primarily formed in the LPF and consumed at the DF, resulting in the accumulation of NO in the region between the LPF and DF. The rapid and monotonic increase in NO emissions within the domain is attributed to the fast propagation of the LPF and the slow propagation of the DF, which is governed by turbulence eddy motion in the mixing layer.

The total mass of N_2O in the domain exhibits a rapid increase during Stage 2 (the ignition stage). Thereafter, it remains nearly constant. As shown in Fig. 8, N_2O in Case H09 distributes in a thin layer at

the LPF and a relatively thick layer near the RPF, where ammonia in the fuel-rich mixture is partially oxidized, leading to the formation of combustion intermediates including N_2O. In LPF, N_2O primarily acts as an intermediate product during ammonia combustion, with its distribution in a narrow region closely following the LPF. As a result, LPF contributes minimally to net N_2O emissions. The net increase in N_2O emissions is mainly attributed to the RPF (cool flames) in the fuel-rich mixtures (see Supplementary Materials S4 for details). Given that the cool flames spread rapidly during the ignition and early back-support stages, N_2O emissions rise sharply in these phases but undergo slow oxidation thereafter.

The impact of turbulence on heat release, NO, and N_2O emissions can be analyzed by comparing the 1D case (L09) and the 3D case (H09). The 1D case (L09) exhibits HRR and NO and N_2O profiles similar to those of Case H09. However, the HRR and NO formation rates in the 1D case are significantly lower than in Case H09. This difference is attributed to both the higher local displacement speed, as shown in Fig. 11, and the highly wrinkled LPF front in the 3D case, cf. Fig. 8, which enhances ammonia consumption and consequently increases HRR and NO formation at the LPF. The formation of N_2O primarily occurs in the cool flames during the ignition stage. The difference in N_2O formation between Cases L09 and H09 is relatively minimal and remains consistent throughout the later stages of combustion.

The impact of jet velocity on heat release and emissions of NO and N_2O is significant. Comparing the u_{jet} = 10 m/s case (J09) with the u_{jet} = 0 case (H09), the peak HRR is higher, and the back-supported flame propagation stage (Stage 3) of Case J09 is delayed with a longer duration, as discussed earlier. The emissions of N_2O are also notably higher. As shown in Fig. 10, the formation of N_2O at the LPF remains confined to a thin layer, similar to that in the u_{jet} = 0 case. However, in the fuel-rich region, where partial oxidation of NH_3 occurs, the N_2O formation layer (at the cool flames) is significantly broader in the u_{jet} = 10 m/s case. Differing from the no-jet case (H09), Case J09 exhibits a decrease in N_2O during the later stage of combustion (t > 1.5 ms). This decrease is attributed to the N_2O consumption reaction $H + N_2O \rightarrow OH + N_2$ in the RAOL, cf. Fig. 9b and Fig. S6.

The formation of NO in the u_{jet} = 10 m/s case is faster in Stage 2 due to the propagation of the ignition kernels, as reflected in the higher peak HRR at the end of Stage 2. Thereafter, NO emissions increase over time but at a slower rate compared to the u_{jet} = 0 case. This is primarily due to the enhanced turbulence mixing, which accelerates the propagation of the DF layer toward the ambient mixture, leading to a faster consumption of NO at the DF.

3.5. Discussions

It is worth noting that the 3D DNS simulations in this study are limited to a specific operating condition (ϕ_{NH_3} = 0.9), utilize only one chemical kinetic mechanism [37], and are performed within a highly customized domain without accounting for compression effects due to computational constraints. While the major findings are expected to be representative and broadly applicable, these limitations should be clearly acknowledged.

Multi-layer flame structures are anticipated to arise under a broader range of conditions with varying ϕ_{NH_3}. However, leaner mixtures (lower ϕ_{NH_3}) are expected to result in slower flame propagation, necessitating increased support from C_7H_{16} in such cases.

The underlying physics is expected to remain consistent across a wider range of operating conditions with different ambient ammonia/air ϕ_{NH_3} values. Even when alternative reaction mechanisms are employed, the same fundamental phenomena should emerge, although quantitative details may vary. For instance, NO is expected to form between the LPF and DF regions regardless of the mechanism used, although peak concentrations may differ.

To extend these findings to more realistic scenarios, compression effects must be incorporated. It is anticipated that the thermophysical processes in a realistic constant-volume chamber will resemble those observed in the current constant-pressure simulations, at least during the early stages of the RCCI combustion process. However, as the LPF propagates and generates significant heat, auto-ignition of the ambient ammonia/air mixture may occur once pressure and temperature rise sufficiently due to compression. These aspects will be investigated further in our future research.

4. Concluding remarks

This study presents a detailed numerical investigation of ignition, reaction modes, and NO/N_2O emissions in ammonia/n-heptane combustion under RCCI engine conditions. The DNS configuration consists of a temporally evolving jet, where cold n-heptane is injected into a hot, premixed ammonia/air ambient with a temperature of 900 K and a pressure of 60 bar. The results reveal various reaction layers and combustion modes, including ignition, cool flames, back-supported premixed flame propagation, freely propagating premixed flames, and diffusion flames. The interactions between different reaction layers affect the formation and consumption of NO and N_2O. The findings provide insights into combustion processes and NO/N_2O emissions in diesel/ammonia RCCI engines. In more detail, the following conclusions are drawn and categorized into the ignition, reaction zone structure and combustion modes, back-supported flame propagation, and NO/N_2O emissions.

Ignition. The onset of ignition occurs in the mixing layer of the ambient ammonia/air and n-heptane streams. The most favorable mixture for ignition is located in the core of the vortex, where the scalar dissipation rate is low. Ignition begins with n-heptane low-temperature ignition reactions and, after a short time, transitions to high-temperature ignition reactions. The jet-induced vortex and turbulence have the effect of delaying the transition from low-temperature to high-temperature ignition, thereby prolonging the ignition process. Additionally, the equivalence ratio of the ambient ammonia/air mixture influences the onset of both low-temperature and high-temperature ignition—the ignition is further delayed as the equivalence ratio of the ambient ammonia/air mixture increases.

Reaction zone structure and combustion modes. Multiple reaction layers exist in the later stages of n-heptane/ammonia RCCI combustion. These layers correspond to the LPF, RPF, DF, and RAOL. The LPF propagates into the ambient ammonia/air mixture, playing a critical role in combustion efficiency in RCCI combustion. The RPF propagates into the rich n-heptane/ammonia/air mixture due to the low-temperature ignition of n-heptane, known as the cool flame. In the RAOL, ammonia remaining from the RPF is oxidized, forming combustion intermediates such as H_2, NH_2, and NH. At the DF, these combustion intermediates are further oxidized by oxidizers left from the LPF.

Back-supported flame propagation. The back-supported LPF propagation is driven by three primary physical and chemical mechanisms: (1) the mixing of highly reactive n-heptane with the ammonia/air mixture, (2) the transfer of heat, radicals, and intermediate species from combustion in the DF, and (3) enhanced mixing driven by jet-induced turbulence and large-scale vortices in the mixing layer. As the LPF moves further into the unburned ammonia/air mixture, the back-support effect weakens, causing its propagation speed to approach that of a homogeneous mixture. The back-support effect can be enhanced by increasing the n-heptane jet velocity.

NO/N_2O emissions. The formation of NO in ammonia/n-heptane RCCI combustion primarily occurs in the LPF, while its consumption takes place in the DF. N_2O is formed primarily in the cool flames in the fuel-rich mixtures. As the n-heptane jet velocity increases, the enhanced vortex and turbulence improve the mixing of the rich n-heptane/ammonia/air mixture with the ambient ammonia/air mixture. This leads to a faster propagation of the DF toward the LPF, accelerating NO consumption and reducing NO emissions. However, a higher n-heptane jet velocity causes delayed ignition and greater entrainment of ambient ammonia into the n-heptane region. This enhances N_2O formation in the fuel-rich mixtures, leading to increased N_2O emissions.

CRediT authorship contribution statement

Yuchen Zhou: Writing – original draft, Visualization, Validation, Software, Methodology, Investigation, Formal analysis, Data curation. **Shijie Xu:** Writing – original draft, Validation, Software, Methodology, Investigation, Formal analysis, Conceptualization. **Leilei Xu:** Writing – original draft, Validation, Software, Methodology, Investigation, Formal analysis, Conceptualization. **Xue-Song Bai:** Writing – original draft, Validation, Supervision, Resources, Project administration, Methodology, Investigation, Funding acquisition, Formal analysis, Conceptualization.

Declaration of competing interest

The authors declare that they have no known competing financial interests or personal relationships that could have appeared to influence the work reported in this paper.

Acknowledgments

This work was supported partly by the Swedish Research Council (VR 2022-05060) and the Hi-EFECTS project, funded by Nordic Energy Research, Norway within the Nordic Grand Solutions Programme. The computations were enabled by resources provided by NAISS at NSC and PDC, as well as the LUMI supercomputer, owned by the EuroHPC Joint Undertaking, hosted by CSC (Finland) and the LUMI consortium. Yuchen Zhou is partially funded by the China Scholarship Council (CSC).

Appendix A. Supplementary data

Supplementary material related to this article can be found online at https://doi.org/10.1016/j.combustflame.2025.114352.

References

[1] W.H. Avery, A role for ammonia in the hydrogen economy, Int. J. Hydrog. Energy 13 (12) (1988) 761–773.
[2] Ravikumar Jayabal, Ammonia as a potential green dual fuel in diesel engines: A review, Process. Saf. Environ. Prot. (2024).
[3] Ernest S. Starkman, HK Newhall, R. Sutton, T. Maguire, L. Farbar, Ammonia as a spark ignition engine fuel: theory and application, Sae Trans. (1967) 765–784.
[4] Christian Sandersen Mørch, Andreas Bjerre, Morten Piil Gøttrup, Spencer C. Sorenson, Jesper Schramm, Ammonia/hydrogen mixtures in an SI-engine: Engine performance and analysis of a proposed fuel system, Fuel 90 (2) (2011) 854–864.
[5] Thomas J. Pearsall, Charles G. Garabedian, Combustion of anhydrous ammonia in diesel engines, SAE Trans. (1968) 3213–3221.
[6] Leilei Xu, Shijie Xu, Xue-Song Bai, Juho Aleksi Repo, Saana Hautala, Jari Hyvönen, Performance and emission characteristics of an ammonia/diesel dual-fuel marine engine, Renew. Sustain. Energy Rev. 185 (2023) 113631.
[7] Aaron J. Reiter, Song-Charng Kong, Demonstration of compression-ignition engine combustion using ammonia in reducing greenhouse gas emissions, Energy Fuels 22 (5) (2008) 2963–2971.
[8] Aaron J. Reiter, Song-Charng Kong, Combustion and emissions characteristics of compression-ignition engine using dual ammonia-diesel fuel, Fuel 90 (1) (2011) 87–97.
[9] Yoichi Niki, Yoshifuru Nitta, Hidenori Sekiguchi, Koichi Hirata, Diesel fuel multiple injection effects on emission characteristics of diesel engine mixed ammonia gas into intake air, J. Eng. Gas Turbines Power 141 (6) (2019) 061020.
[10] Amin Yousefi, Hongsheng Guo, Shouvik Dev, Brian Liko, Simon Lafrance, Effects of ammonia energy fraction and diesel injection timing on combustion and emissions of an ammonia/diesel dual-fuel engine, Fuel 314 (2022) 122723.
[11] Amin Yousefi, Hongsheng Guo, Shouvik Dev, Simon Lafrance, Brian Liko, A study on split diesel injection on thermal efficiency and emissions of an ammonia/diesel dual-fuel engine, Fuel 316 (2022) 123412.
[12] Niels Førby, Thomas B. Thomsen, Rasmus F. Cordtz, Frantz Bræstrup, Jesper Schramm, Ignition and combustion study of premixed ammonia using GDI pilot injection in CI engine, Fuel 331 (2023) 125768.
[13] Hongsheng Guo, Brian Liko, David Stevenson, Kevin Austin, An experimental investigation on combustion and emissions of a hydrogen enriched ammonia–diesel dual fuel engine at a medium load condition, J. Eng. Gas Turbines Power 147 (9) (2025).
[14] Rolf D. Reitz, Ganesh Duraisamy, Review of high efficiency and clean reactivity controlled compression ignition (RCCI) combustion in internal combustion engines, Prog. Energ. Combust. Sci. 46 (2015) 12–71.
[15] Yongzhong Huang, Lin Lyu, Junjie Liang, He Yang, Neng Zhu, Hao Sang, Xintang Zhang, Performance and emission characteristics of marine ammonia/diesel dual-fuel engines at different diesel substitution rates, Fuel 379 (2025) 132967.
[16] Liang Zheng, Jinhe Zhang, Li Huang, Xiaoxing Tan, Hongmei Li, Jiaying Pan, Mingzhi Feng, Experimental study on ignition and flame propagation of premixed ammonia ignited by direct-injected diesel in an optical rapid compression machine, Fuel 378 (2024) 132887.
[17] Xiaochen Wang, Han Bu, Hao Chen, Jinlong Liu, Zhenbin Chen, Jianbing Gao, Numerical investigation of diesel spray combustion characteristics in the ammonia/air atmosphere, J. Energy Inst. 116 (2024) 101718.
[18] Rui Ding, Yaopeng Li, Haoran Li, Yikang Cai, Ming Jia, Effects of ammonia energy ratio and PODE injection timing on combustion and emissions in a PODE/ammonia RCCI engine, Fuel 378 (2024) 132924.
[19] Shouzhen Zhang, Qinglong Tang, Haifeng Liu, Rui Yang, Mingfa Yao, Numerical investigation and optimization of the ammonia/diesel dual fuel engine combustion under high ammonia substitution ratio, J. Energy Inst. 117 (2024) 101797.
[20] Liang Yu, Wei Zhou, Yuan Feng, Wenyu Wang, Jizhen Zhu, Yong Qian, Xingcai Lu, The effect of ammonia addition on the low-temperature autoignition of n-heptane: An experimental and modeling study, Combust. Flame 217 (2020) 4–11.
[21] Juan Ou, Zunhua Zhang, Zhentao Liu, Jinlong Liu, Effect of ammonia reaction kinetics on the two-stage ignition mechanism of dimethyl ether, Fuel Process. Technol. 261 (2024) 108112.
[22] Ziwei Huang, Haiou Wang, Kun Luo, Jianren Fan, Direct numerical simulation of ammonia/n-heptane dual-fuel combustion under high pressure conditions, Fuel 367 (2024) 131460.
[23] Leilei Xu, Xue-Song Bai, Numerical investigation of engine performance and emission characteristics of an ammonia/hydrogen/n-heptane engine under RCCI operating conditions, Flow. Turbul. Combust. 112 (3) (2024) 957–974.
[24] Takuya Tomidokoro, Takeshi Yokomori, Hong G. Im, Numerical study on propagation and NO reduction behavior of laminar stratified ammonia/air flames, Combust. Flame 241 (2022) 112102.
[25] Cheng Chi, Dominique Thévenin, DNS study on reactivity stratification with prechamber H2/air turbulent jet flame to enhance NH3/air combustion in gas engines, Fuel 347 (2023) 128387.
[26] Zhiyan Wang, John Abraham, Fundamental physics of flame development in an autoigniting dual fuel mixture, Proc. Combust. Inst. 35 (1) (2015) 1041–1048.
[27] Jiun Cai Ong, Kar Mun Pang, Rajavasanth Rajasegar, Ales Srna, Xue-Song Bai, Jens H. Walther, LES of pilot n-heptane ignition and its interaction with the lean premixed methane–air mixture in a dual-fuel combustion engine, Proc. Combust. Inst. 40 (1–4) (2024) 105281.
[28] Gwang Hyeon Yu, Minh Bau Luong, Suk Ho Chung, et al., Ignition characteristics of a temporally evolving n-heptane jet in an iso-octane/air stream under RCCI combustion-relevant conditions, Combust. Flame 208 (2019) 299–312.
[29] Ankit Bhagatwala, Ramanan Sankaran, Sage Kokjohn, Jacqueline H. Chen, Numerical investigation of spontaneous flame propagation under RCCI conditions, Combust. Flame 162 (9) (2015) 3412–3426.
[30] Shijie Xu, Shenghui Zhong, Kar Mun Pang, Senbin Yu, Mehdi Jangi, Xue-Song Bai, Effects of ambient methanol on pollutants formation in dual-fuel spray combustion at varying ambient temperatures: A large-eddy simulation, Appl. Energy 279 (2020) 115774.
[31] Wanhui Zhao, Guiqiang Li, Ting Sun, Ying Zhang, Lei Zhou, Haiqiao Wei, Numerical study on the ignition and flame propagation of ammonia/n-heptane dual fuels, Energy Fuel 37 (17) (2023) 13354–13365.
[32] Evatt R. Hawkes, Ramanan Sankaran, James C. Sutherland, Jacqueline H. Chen, Scalar mixing in direct numerical simulations of temporally evolving plane jet flames with skeletal CO/H2 kinetics, Proc. Combust. Inst. 31 (1) (2007) 1633–1640.
[33] Evatt R. Hawkes, Obulesu Chatakonda, Hemanth Kolla, Alan R. Kerstein, Jacqueline H. Chen, A petascale direct numerical simulation study of the modelling of flame wrinkling for large-eddy simulations in intense turbulence, Combust. Flame 159 (8) (2012) 2690–2703.
[34] Alex Krisman, Evatt R. Hawkes, Jacqueline H. Chen, A parametric study of ignition dynamics at ECN spray a thermochemical conditions using 2D DNS, Proc. Combust. Inst. 37 (4) (2019) 4787–4795.
[35] Shenghui Zhong, Fan Zhang, Mehdi Jangi, Xue-Song Bai, Mingfa Yao, Zhijun Peng, Structure and propagation of n-heptane/air premixed flame in low temperature ignition regime, Appl. Energy 275 (2020) 115320.
[36] Ning Zhang, Fan Zhang, Shenghui Zhong, Zhijun Peng, Jiangfei Yu, Haifeng Liu, Cangsu Xu, Numerical and theoretical investigation of ethanol/air flame instability, Combust. Theor. Model. 24 (6) (2020) 1108–1129.
[37] Leilei Xu, Yachao Chang, Mark Treacy, Yuchen Zhou, Ming Jia, Xue-Song Bai, A skeletal chemical kinetic mechanism for ammonia/n-heptane combustion, Fuel 331 (2023) 125830.

[38] Jacqueline H. Chen, Alok Choudhary, Bronis De Supinski, Matthew DeVries, Evatt R. Hawkes, Scott Klasky, Wei-Keng Liao, Kwan-Liu Ma, John Mellor-Crummey, Norbert Podhorszki, et al., Terascale direct numerical simulations of turbulent combustion using S3D, Comput. Sci. Discov. 2 (1) (2009) 015001.

[39] Marc T. Henry de Frahan, Lucas Esclapez, Jon Rood, Nicholas T. Wimer, Paul Mullowney, Bruce A. Perry, Landon Owen, Hariswaran Sitaraman, Shashank Yellapantula, Malik Hassanaly, et al., The pele simulation suite for reacting flows at exascale, in: Proceedings of the 2024 SIAM Conference on Parallel Processing for Scientific Computing, PP, SIAM, 2024, pp. 13–25.

[40] Olivier Desjardins, Guillaume Blanquart, Guillaume Balarac, Heinz Pitsch, High order conservative finite difference scheme for variable density low Mach number turbulent flows, J. Comput. Phys. 227 (15) (2008) 7125–7159.

[41] Lucas Gasparino, Filippo Spiga, Oriol Lehmkuhl, SOD2D: A GPU-enabled spectral finite elements method for compressible scale-resolving simulations, Comput. Phys. Comm. 297 (2024) 109067.

[42] Henry J. Curran, Paolo Gaffuri, William J. Pitz, Charles K. Westbrook, A comprehensive modeling study of n-heptane oxidation, Combust. Flame 114 (1–2) (1998) 149–177.

[43] N. Peters, G. Paczko, R. Seiser, K. Seshadri, Temperature cross-over and non-thermal runaway at two-stage ignition of n-heptane, Combust. Flame 128 (1–2) (2002) 38–59.

[44] ECN, Engine combustion network modeling standards and recommendations, 2025, https://ecn.sandia.gov/diesel-spray-combustion/computational-method/modeling-standards/, (Accessed January 2025).

[45] Epaminondas Mastorakos, Ignition of turbulent non-premixed flames, Prog. Energy Combust. Sci. 35 (1) (2009) 57–97.

[46] Yiguang Ju, Christopher B. Reuter, Omar R. Yehia, Tanvir I. Farouk, Sang Hee Won, Dynamics of cool flames, Prog. Energy Combust. Sci. 75 (2019) 100787.

[47] Vladimir A. Alekseev, Elna J.K. Nilsson, Reduced kinetics of NH3/n-heptane: Model analysis and a new small mechanism for engine applications, Fuel 367 (2024) 131464.

[48] Bowen Wang, Shijun Dong, Zuozhou Jiang, Wenxue Gao, Zhongxuan Wang, Jianwei Li, Can Yang, Zhaowen Wang, Xiaobei Cheng, Development of a reduced chemical mechanism for ammonia/n-heptane blends, Fuel 338 (2023) 127358.

[49] W. Yang, K.K.J. Ranga Dinesh, K.H. Luo, D. Thevenin, Direct numerical simulation of turbulent premixed ammonia and ammonia-hydrogen combustion under engine-relevant conditions, Int. J. Hydrog. Energy 47 (20) (2022) 11083–11100.